Research Article

Nano Research
2023, 16(5): 7470–7480

ISSN 1998-0124 CN 11-5974/O4
https://doi.org/10.1007/s12274-022-5355-3

Diffusion dynamics and characterization of attogram masses in optically trapped single nanoparticles using laser-induced plasma imaging

Pablo Purohit[†], Francisco J. Fortes, and Javier Laserna (✉)

UMALASERLAB, Departamento de Química Analítica, Universidad de Málaga, C/Jiménez Fraud 4, Malaga 29010, Spain
[†] Niels Bohr Institute, University of Copenhagen, Blegdamsvej 17, 2100 Copenhagen, Denmark

Received: 13 September 2022 / **Revised:** 23 November 2022 / **Accepted:** 24 November 2022

ABSTRACT

In the present work, a wavelength-selected plasma imaging analysis system is presented and used to track photons emitted from single-trapped nanoparticles in air at atmospheric pressure. The isolated nanoentities were atomized and excited into plasma state using single nanosecond laser pulses. The use of appropriate wavelength filters alongside time-optimized acquisition settings enabled the detection of molecular and atomic emissions in the plasma. The photon detection efficiency of the imaging line resulted in a signal > 400 times larger than the simultaneously-acquired dispersive spectroscopy data. The increase in sensitivity outlined the evolution of diverse physicochemical processes at the single particle scale which included heat and momentum transfer from the plasma into the particle as wells as chemical reactions. The imaging detection of excited fragments evidenced different diffusion kinetics and time frames for atoms and molecules and their influence upon both the spectroscopic emission readout and fabrication processes using the plasma as a reactor. Moreover, the origin of molecular species, whether naturally-occurring or derived from a chemical reaction in the plasma, could also be studied on the basis of compositional gradients found on the images. Limits of detection for the inspected species ranged from tens to hundreds attograms, thus leading to an exceptional sensing principle for single nanoentities that may impact several areas of science and technology.

KEYWORDS

single nanoparticle inspection, wavelength-selected laser-induced plasma imaging, laser fabrication, attogram characterization, atomic/molecular diffusion

1 Introduction

As the power and helpfulness of single nanoparticles (NPs) are further evidenced by diverse applications of extreme finesse [1–4], techniques capable of performing the physicochemical inspection of these entities gain further relevance. Laser-based techniques, owing to their versatility, have attracted the interest of researchers seeking to adapt the advantages found for in-bulk inspection to the own complexity of the nanoscale. As a recent example of the great sensitivity displayed by these techniques, Mie resonance spectroscopy and mass spectrometry were successfully combined for evidencing organic chemical processes occurring on the surface of single aerosolized multicomponent particles. The proposed methodology was capable of tracking subtle size changes induced on the particles as a consequence of these reactions. The minimum detectable diameter variation reported was 5 nm [5]. Such an application is likely to increase the interest in the use of the surface of discrete particles as nanoreactors. Furthermore, irradiated upconverting nanoparticles have been used to detect Cu^{+2} with unprecedented signal-to-noise ratios (SNR) [6]. Tracking the laser-induced response of these recently-developed nanoprobes may expose complex mechanisms in full detail [7, 8]. In the field of optical emission techniques, the combination of optical catapulting (OC), optical trapping (OT), and laser-induced breakdown spectroscopy (LIBS) has been demonstrated to yield the extreme sensitivity required for the inspection of single nanoparticles coming from dry aerosols in air at atmospheric pressure. This analytical platform, OC-OT-LIBS, was employed to detect and characterize absolute masses in the sub-femtogram range of particles isolated in an optical radiation pressure field down to 25 nm [9]. One of the most significant contributions of LIBS in nanoinspection is the simultaneous detection of multiple elements in a single laser event, exposing the entire qualitative composition of the NP and, potentially, on a quantitative level [10]. LIBS has exhibited outstanding synergy with OT as the trap characteristics can be tuned to work exclusively with specific NP morphologies to create a size- and shape-selective tool [11]. A main drawback associated to dispersive spectroscopies such as LIBS is that a significant fraction of the photons emitted by the sample are lost in their way to the detector as they traverse the different optics of the detection line. This fact decreases the sensitivity of dispersive approaches hindering the chemical characterization of scarce quantities and their application in nanoinspection. Furthermore, other tracking capabilities of the sensor (such as spatial resolution) are also commonly hindered due to the required layout of the instruments, thus restricting the amount of information that can be extracted from each inspection

Address correspondence to laserna@uma.es

events [9–11]. Direct imaging of the plasmas generated upon particle inspection using wavelength filters to specifically select the collected light is a plausible solution. The number of interfaces required to record the plasma emission decreases whereas physico-chemical information regarding the sample is still provided. Moreover, plasma imaging allows for a greater spatial resolution with a relatively straightforward interpretation of the possible reasons motivating compositional gradients in the plasma within a single captured frame. LIBS imaging is a well-established methodology in a number of application fields within LIBS community such as the chemical characterization of catalysts [12] or biopsied tissues [13, 14]. Despite the increasing popularity of LIBS imaging and the development of advanced data processing schemes [15], the direct analysis of laser-induced plasma plumes remains to be further exploited. Until now, reported results suggested direct plasma imaging analysis as an effective method for understanding processes such as the evolution/diffusion of analytes, chemical dissociations originated from heat exchange within the plasma or to expose the mechanisms causing the excitation of atoms to emissive states [16, 17]. In addition, the fact that plasma imaging has been successfully used to probe particles in wet aerosols also motivates attempting to apply the approach to enhance the performance of OC-OT-LIBS [18].

In the present work, a wavelength-selected laser-induced plasma plume imaging line, from now on referred to as λP or λP-imaging, is integrated within the OC-OT-LIBS analytical platform, allowing to acquire plasma images of single optically-trapped micro- and nanoparticles in air at a given wavelength. Different chemical species featuring a variety of mean diameters were inspected, 70 and 25 nm Cu NPs, 90 nm $CuFe_2O_4$ ferrites, and 2 μm graphite particles, by setting in the λP-imaging line either a bandpass (BP) filter, a line filter or a combination of both. From the inspection of microspheres, the instrumental approach and the data processing procedure were validated before testing the analytical performance of the methodology on the more extreme scenario of single nanoparticle characterization. The cooperation between both detection schemes is evaluated to assess the a priori positive feedback in the λP-LIBS combination for lowering the detection limits in the analysis of single nanoentities while also resulting in a better comprehension of the particle–plasma interaction as well as how thermodynamics guides the process and conditions the generated readout by means of momentum transference into the particle.

2 Results and discussion

2.1 Working principle and inspection of single graphite microparticles using wavelength-resolved laser-induced plasma imaging

Figure 1 schematizes the combination of the OC-OT-LIBS platform and the λP imaging line for the reported experiments along its working principle. In the instrument used herein, particles isolated within the volume of the optical trap were excited into plasma state using a single laser pulse of 6 nanoseconds in duration. Light emitted from the plasma was recorded via two different detection lines at the same time. LIBS inspection was performed by an optical fiber connected to the entrance of a dispersive spectrometer equipped with a charge-coupled device (CCD) detector. The spectroscopic line yielded spectra featuring emission lines from the different chemical species composing the plasma, therefore indicating the optimum wavelength filters to perform the imaging analysis. On the other hand, plasma images were acquired by an intensified CCD (iCCD) camera. Appropriated filters suppressed wavelengths other than those of analytical interest before being focused into the camera and producing the wavelength-selected images used for further data analysis. A full description of the instrument and the optics is provided in the Methods section. The transmission curves of the filters employed for the λP analysis are shown in Fig. S1 in the Electronic Supplementary Material (ESM). The main emission lines used for the inspection of single particles were Cu(I) at 324.75 nm (for Cu and $CuFe_2O_4$ nanospheres) and the CN violet system at 388.30 nm (corresponding to the transit (0,0) of the molecular band). The physical properties of the samples are summarized in Table S1 in the ESM. Materials were placed upon 200 μm-thick glass slides and then covered by a quartz cuvette of 10 mm optical path glued to the slide to prevent sample losses. Particles were trapped using visible light, 532 nm, thus producing trackable scattering used to assess their position along the experiment's z axis via simultaneous orthogonal complementary metal oxide semiconductor (CMOS) and iCCD visualization. Particle position could be manipulated for distances up to 2 mm (depending on particle size) for precise adjustment at the zero coordinate, to which every optical element of the analytical platform was aligned (see Methods section). LIBS spectra were recorded simultaneously with the plasma images. The feedback from the cross-linked information provided by both lines guided the decision to keep (single particle) or discard (clustered particles) the image associated to a given inspected event. For this purpose, a statistic sorting scheme based on recorded LIBS net intensities and the standard deviation of the data was used as the spectroscopic readout is directly proportional to the particle mass and, ultimately, to their size [9]. This approach, fully described in the Methods section, established an experimental net intensity range that accounted for the inherent size dispersion of the employed samples. Individually inspected particles were expected to produce signals over the intensity frame resulting from the sorting scheme [9, 10, 11, 20]. Therefore, only those images from events in compliance with the sorting method were considered for further λP analysis. In the case of graphite, the analyzing laser was focused 1 mm away from the zero coordinate where the microsphere was stably trapped. The adjustment of the laser focus position reduced the contribution of ionized air (mainly in the form of N_2, N^+, and O(I) emissions in the 389–395 nm spectral region) in both datasets, LIBS and λP-imaging acquisition [19]. As plasma–particle interaction is the primary mechanism leading to both particle atomization and dissociation in single-particle LIBS (SP-LIBS), the use of laser beam energy above the air plasma formation threshold is mandatory [9, 19, 20].

The concomitant air plasma acts as laser energy storage and transfers part of the energy excess as heat into the trapped particle, which becomes engulfed by the plasma during its expansion. In return, the particle cedes mass into the plasma, both processes being rate-limited, which is subsequently excited into spectroscopically emissive states [10, 11]. To evaluate the performance of λP, images from single trapped particles were acquired until signal extinction. The integration time (w) was 100 ns, while the acquisition delay (d) was incremented in steps of 100 ns to capture different moments of the plasma lifespan. The d value refers to the time that elapsed from the laser event until signal acquisition by the iCCD camera begins. The w value ensured the collection of enough light while keeping fluctuations influenced by the evolution of plasma emission to a minimum, thus facilitating data interpretation. Figure 2(a) shows the most relevant wavelength-filtered unprocessed images recorded for the 2 μm graphite spheres. The entire series is shown in Fig. S2 in the ESM. Upon ignition, a bright core was formed at the laser focus position featuring the contribution from the air ionization. The average spectrum from this core is presented in Fig. S3 in the

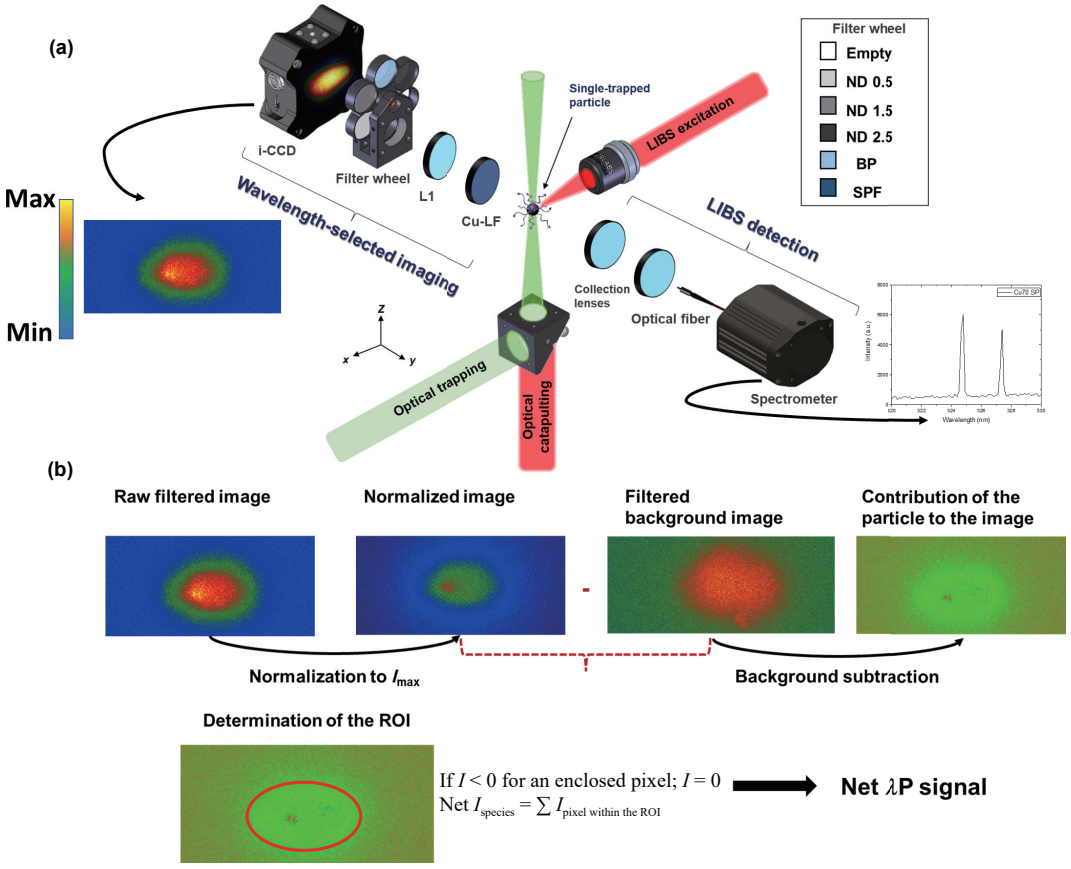

Figure 1 Working principle and scheme for both employed detection lines. (a) 3D diagram of the λP-LIBS setup employed for chemical analysis of single-trapped particles. Filter selection was based on the target plasma emission. Legend details the optics mounted upon the filter wheel with ND indicating neutral density filters, BP being the bandpass filter for CN emission monitoring, and the SPF being the shortpass filter required to suppress the background when tracking the Cu line. The filter denoted as Cu-LF was only present in the optical train for detection of Cu NPs. Cu-LF is a line filter that, upon 5° rotation, allowed only light at 324.75 nm and in the range of 400–900 nm to go through, then SPF cut the latter portion of the radiation before it was focused by lens L1 and reached the iCCD camera. (b) Image processing scheme for an example raw filtered image until extraction of the net intensity for the particle signal. For better visualization of the temporal evolution of the signal, images were normalized to the intensity maximum of the time series, yet raw intensity values were used for background subtraction and net signal extraction.

ESM. As time passed, the laser-induced plasma expanded in the *x*-axis, eventually reaching the trapped particle and occluding it. At 600 ns, a second plasma core appeared at the particle spot. As stated above, the rate-limited nature of the energy–mass exchange process could explain the observed delay between the arrival of the plasma at the zero coordinate and the plasma particle formation (see *d*: 400–600 ns in Fig. S2 in the ESM). Each image shown in both Fig. 2(a) and Fig. S2 in the ESM corresponds to different laser events. Thus, minor variations in the general trend were present owing to uncertainties associated to particle size dispersion (see samples in the Methods section), particle position fluctuations within the optical trap (i.e., Brownian motion), and the intrinsic variability of the laser–air interaction. From 600 ns, the particle lobe expanded in radius and decayed at a different rate as different predominant chemical species populated each core. In λP analysis, given the transmission profile of the bandpass filter used, the air lobe was mainly composed of excited O atoms and a minor contribution from N^+ ions emitting at 399.5 nm. Contrarily, as shown by LIBS spectra in Fig. S3 in the ESM, the particle lobe was composed almost exclusively of CN radical. Control experiments presented in Fig. S3 in the ESM also confirm that the two lobes structure could only be observed when particles were occluded in the optical trap. This observation, alongside the lobes' spectral differences, further confirms its link to the microparticle.

Different chemical compositions of the cores were further evidenced by the temporal evolution of the lobe aspect ratio shown in Fig. 2(b). The graphite-related section became consistently larger immediately after the onset of the signal, with its intensity lasting longer than that of the air lobe. The two main reasons for this observation are the time it takes for the CN radical to form in comparison with that required for dissociating O_2 and N_2 and exciting the free atoms and, also, the different emission lifetimes for each species, with ions and atoms featuring a faster decay when compared to molecules.

Under our experimental conditions, the main formation route for CN radical was the recombination of free C atoms with dissociated atmospheric nitrogen [21, 22]. These results are consistent with those presented in Fig. 2(b) and Fig. S2 in the ESM (*d*: 1400–2000 ns). The molecular emission appeared later and lasted for longer, thus explaining the slower decay of the graphite lobe compared to the air one, which extinguished at 1800 ns (Fig. S2 in the ESM). Therefore, the observed decay of the air lobe is due to the atomic species featuring emissions lines within the spectral range of the bandpass filter becoming extinguished. Moreover, these results further reinforced the plasma–particle interaction governing the atomization and excitation process. Figure 2(c) plots the position of the plasma front, that is, the air plasma expansion along the *x*-axis in the time-resolved λP image series. Plasma position stagnated upon reaching the trapped particle and its velocity decayed exponentially due to the loss of its supersonic expansion features at early lifetimes. The observation implies that additional air ionization favored the energy transfer into the graphite particle over size expansion. The higher thermal conductivity for graphite (400 $W \cdot mK^{-1}$ versus 26.62 $W \cdot mK^{-1}$ for air) is a plausible explanation for the behavior change upon particle interception. Furthermore, low fragment dispersion indicated highly spatially-restrained particle dissociation, which was coherent with the reduced laser–particle interaction imposed

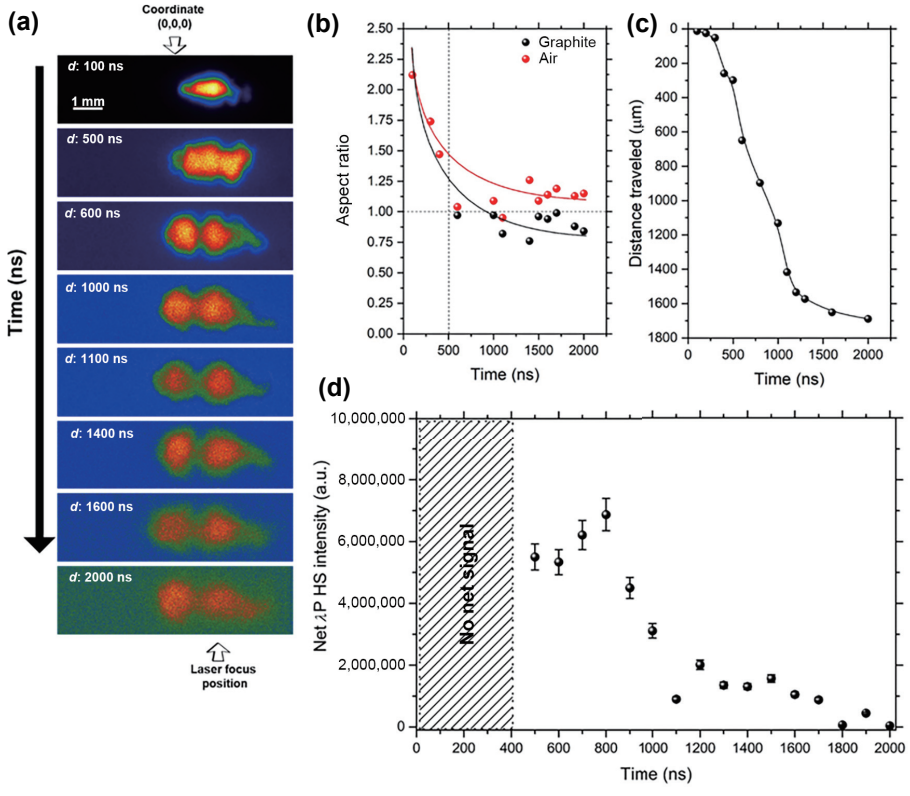

Figure 2 Results of the characterization of graphite microspheres. (a) Temporal evolution of graphite plasmas. Images are background-subtracted. Images were normalized to d = 100 ns for better visualization. Two lobes can be observed, the left one corresponding to the particle and the right one to ionized air at the analyzing laser's focus. (b) Aspect ratio for plasma cores measured from Fig. S2 in the ESM. The sample-related lobe became the larger emissive focus from its inception at d = 500 ns. (c) Distance traveled by the plasma front position as a function of time. (d) λP-imaging intensity temporal evolution. Simultaneously LIBS data are provided in Fig. S4 in the ESM. Data for five single particle events were averaged to calculate results in (b)–(d). Scale bar is 1 mm.

by the out-of-focus excitation scheme used. The lower temperature of the plasma periphery reaching the particle resulted in the chemical reactions yielding the CN radical being preferentially located around the graphite sphere. This contrasts with the radial and axial migration of species prior to the formation of new molecules observed in conventional plasma experiments. The need for relocation to colder coordinates along plasma plumes usually results in a large distribution of the reacting atoms or, in other words, locally low concentrations. Hence, provided the strength of the optical trap is sufficiently high, as in the case described herein, the chemical reactions of the species contained in the particle can be confined to a certain region of interest within the laser-induced plasma. As chemical reactions between the particle and the surrounding atmosphere or another particle can be monitored with λP imaging, the information derived from data analysis can be used to control the temporal evolution of reactions and enhance the yield of target fragments or molecules. In our case, we used the images to determine the time frame of maximum CN radical production in order to quantify its signal and, ultimately, evaluate the lower mass limit that the approach could detect. For quantitative λP analysis, 5 images were acquired at each delay time. Image processing is detailed in the Methods section. The evolution of the CN intensity as a function of time is plotted in Fig. 2(d). The maximum intensity was registered at 800 ns, in agreement with the simultaneously acquired LIBS data (see Methods for data curation and Fig. S4 in the ESM). At the maximum CN emission intensity, a raw signal enhancement of 2 orders of magnitude was found for the λP-imaging analysis. The recorded signal was 6.86×10^6 and 1.6×10^4 a.u. for λP and LIBS, respectively, thus confirming the higher sensitivity provided by λP inspection for the analysis of single microparticles on an arbitrary scale. Owing to the different nature of the detection of both approaches such an increase was expected. To provide the comparison with a quantitative physical implication and translate this finding into an enhanced analytical performance, photon detection and analytical figures of merits are expanded and discussed in Section 2.3, where the interplay between techniques is further exploited.

2.2 Dual analysis of single Cu and Cu-containing nanoparticles

The capabilities of the proposed methodology in a more extreme scenario were also evaluated. For the case of 70 nm Cu NPs, the particle lifetime was expected to be far shorter due to the exiguous sample quantity involved in the analysis [20], 1.61 fg on average. In consequence, the acquisition time for plasma imaging was settled at 250 ns. Time-resolved analysis was performed from 0 ns until copper signal extinction at ~ 1250 ns. Results are plotted in Fig. 3(a). As expected from particle–plasma interaction, NP emission started at later times (d: 500 ns). Background subtraction and resulting threshold-filtered matrices of the images in Fig. 3(a) are presented in Figs. 3(b) and 3(c), respectively. As the Cu core developed, displacements up to 500 μm from the zero coordinate were observed. In contrast to microparticles, the smaller mass of Cu NPs leaded to a more pronounced momentum transfer effect upon particle explosion, causing the spatial relocation of the NP in time. This effect was especially appreciable at 500 ns, where a cloud of Cu atoms diffusing from the central point were observed. Displacements in the detection axis may explain signal fluctuations and eventual loss unrelated to inherent particle traits (i.e., size dispersion causing a fraction of the particle to feature masses below the limit of detection (LOD) value) in SP-LIBS. In such cases, the light emission point may fall beyond the boundaries of habitual optical fiber core diameters used for LIBS collection (typically 0.6 and 1 mm). The possibility of tracking analyte diffusion within the laser-induced plasma is an essential

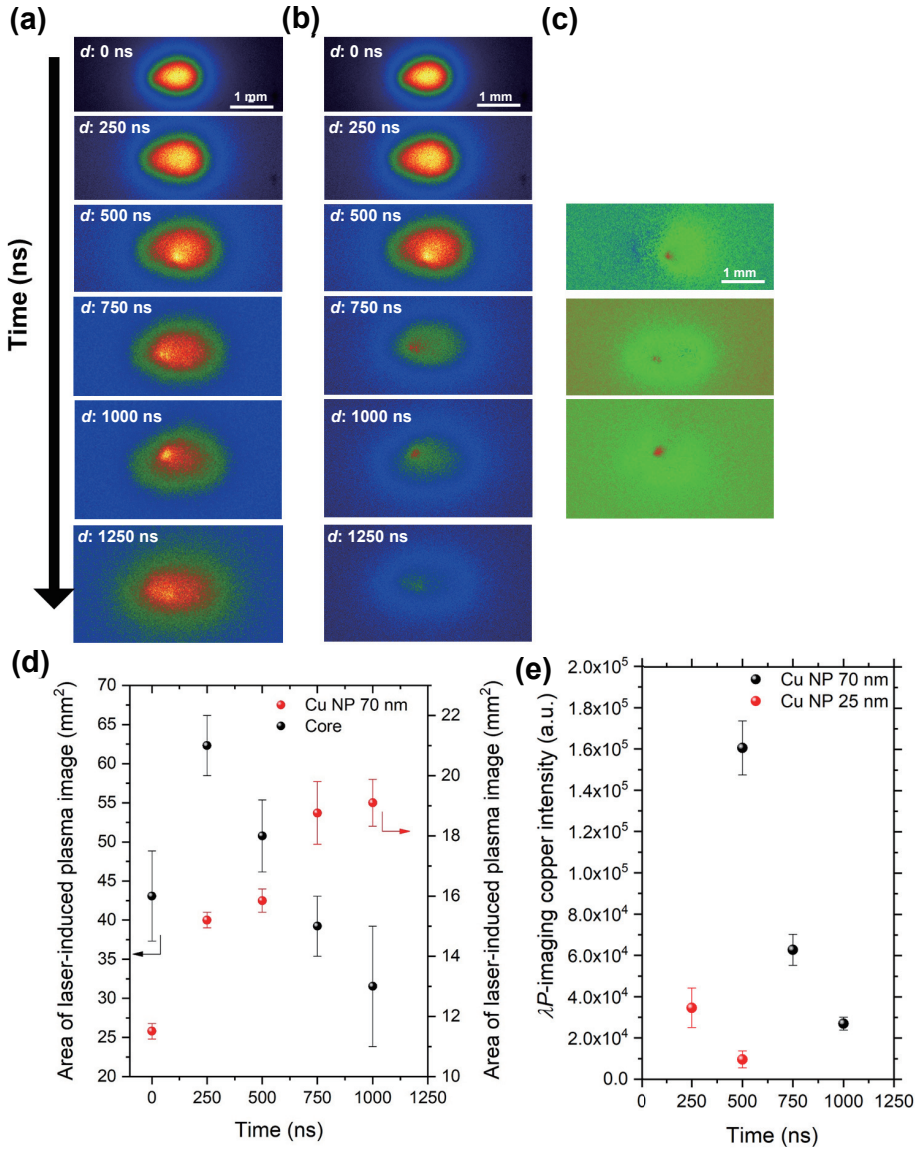

Figure 3 Plasma imaging of single optically-trapped Cu nanoparticles. (a) Time-resolved λP-imaging of copper nanoparticles at 324.75 nm. It should be noted that images are background-subtracted as described in Methods section. Moreover, each frame corresponds to a single laser event. (b) Images presented in (a) normalized the series intensity maximum for better visualization. (c) Fully processed λP images, for data with a SNR value higher than 3, after background correction in (b). (d) Evolution of the NP plasma area against total core size. (e) λP-imaging copper intensity of the images in (c). The graph also features the evolution of the signal for Cu NPs of 25 nm. Owing to their exiguous size, NPs were expected to produce a sudden signal spike followed by an exponential decay as experimentally demonstrated in this vignette. Moreover, smaller particles are easier to dissociate by the plasma, thus yielding earlier signals which also disappear before than those produced by NPs containing a larger quantity of atoms. For each delay value in (d) and (e), five single particle events were acquired.

advantage of the λP approach as the contribution of the out-of-bounds emitting atoms may also be selectively added to the integrated area. Moreover, the study of intra-plasma fractionation, of particular interest for isotopic analysis, may also be further comprehended by direct visualization in the proposed λP methodology. Calculated areas of the Cu core and the air plasma core are shown in Fig. 3(d), indicating an energy transfer into the particle and the presence of different chemical species in both nuclei. Free electrons and ions composing the non-NP related core caused the unspecific Bremsstrahlung radiation responsible for the background observed alongside the Cu signal. The λP-imaging Cu intensity at 324.75 nm as a function of plasma lifetime is plotted in Fig. 3(e). As seen, the maximum intensity was registered at 500 ns, in agreement with previously reported results [20]. Upon comparison to net LIBS signal, $I_{500ns} = 2580 \pm 365$ a.u. (Fig. S5 in the ESM), λP analysis resulted in a 63-fold signal increment, $1.65 \times 10^5 \pm 1.58 \times 10^4$ a.u.

To experimentally survey the limits of λP in terms of sensitivity, we trapped and inspected Cu NPs of 25 nm in diameter following the same procedure described for the 70 nm particles. Net signals for these smaller NPs could only be extracted from the plasma images at d = 250 and 500 ns. Example images for both acquisition delay values are shown in Fig. S6 in the ESM. As shown in Fig. 3(e), the shorter time spawn of the signal from 25 nm Cu NPs is also coherent with the discussion ensued so far. The earlier appearance can be explained on the basis of their smaller size and, therefore, lower content of Cu–Cu bonds, leading to a faster particle dissociation, excitation and, consequently, extinction of the NP emission. Upon comparison of the intensity extracted from the λP images for 25 nm NPs, the signal at the maximum intensity was an order of magnitude below those collected for the particle size of 70 nm. The observed drop was also expected for direct inspection of the plasma given the well-known relation between LIBS signal and the mass of the analyte [9]. From these results, we can conclude that λP imaging is capable of detecting the signal from Cu particles as small as 25 nm featuring a mass of 73 ag. To further verify the sensitivity to mass changes of the λP approach under identical experimental

operation parameters, i.e., excitation energy and collection time settings, copper-containing ferrites ($CuFe_2O_4$) were also tested. The average absolute Cu mass of the 90 nm ferrite particles was ca. 0.55 fg. Figure 4 shows λP images of background-subtracted and gain-corrected $CuFe_2O_4$ plasma images. Upon quantitative data treatment for ferrites, the average LIBS signal was I_{max} = 899 ± 290 a.u. (n = 15) whereas the average λP intensity registered for the multielemental nanomatrices was $6.8 \times 10^4 \pm 2.9 \times 10^4$ a.u. The increased uncertainty found in λP-imaging can be explained by its enhanced sensitivity as slight size variations in the samples translated into more significant signal differences. The average net intensity value for the ferrites was 0.41 times to those recorded for Cu NPs. This data is in good agreement with the ca. 66% drop in Cu quantity featured in the cuprospinel, thus indicating a mass proportionality and the prospective use of λP for quantitative applications on single nanoentities.

A specific source of information that can be extracted from the λP imaging technique is how the chemical bonds present in the particles affect the dissociation and subsequent distribution of the freed species within the laser-induced plasma. It should be noted that in this work each inspected sample feature a different type of chemical bond, i.e., covalent (graphite, Fig. 2(a)), metallic (copper nanoparticles, Fig. 3(c) and Fig. S6 in the ESM), and ionic ($CuFe_2O_4$, Fig. 4). Attending to the reported results, particle displacements from the center of the optical trap and the subsequent distribution of the species were found to vary for each type of sample which suggested characteristic bond-dependent heat and momentum transfer rates. Covalent particles exhibited the least thermophoretic effect as they remained virtually constant at the center of the optical trap. A plausible explanation resides in the fact that graphite spheres lacked direct interaction with the core of the plasma as it was sparked 1 mm away from the OT. Therefore, the microparticles were not exposed to amounts of thermal energy as high as those interacting with the NPs, leading to a less explosive dissociation process. Still, enhanced thermal relaxation and reduced accumulation of internal pressure owing to the larger particle diameters of the microspheres is to be accounted as well to explain their positional stability. Consequently, C atoms concentration was highly localized within the laser-induced plasma and created a preferential region for the formation of the CN molecule, further evidenced by the lack of migration of the molecular emissions. Upon comparison of the Cu-containing particles, as shown in Fig. 4, the diffusion of Cu within ferrite plasmas was more significant than those observed for Cu NPs. The change from metallic Cu–Cu bonds into ionic Cu–O bonds results in a substantial alteration of the thermal attributes of the sample. This fact modifies the conduction capabilities of the ionic structure (weaker than those of the pure metal), leading to a slower and more scattered release of atoms, thus facilitating the observation of their diffusion into the plasma. Contrarily, the faster process experienced by the metallic NPs would be coherent with a strong, localized explosion due to overheating [19, 23, 24]. As a result, most copper fragments remain closer and form the brighter cores observed in Fig. 3(a). Cu NPs dissociated as a whole at positions away from the plasma core due to heat causing them to relocate rather than to accumulate pressure. Owing to their similar sizes, thermal conductivity differences derived from a change in the nature of the bond seem to predominantly justify the increased diffusion of ionic particles when compared to metallic ones. On the other hand, the excess energy exchange process for the ferrites was not as effective. Oxide NPs cracked and dissociated before relocating to the plasma periphery owing to higher internal pressures. Lastly, the implications of particle size in fragment distribution within the laser-induced plasma could also be studied for the metallic particles. Both Cu NPs were observed to dissociate identically with light emission being strongly restricted to a single core, indicating low atomic dispersion. However, for 25 nm Cu particles their faster atomization implied negligible displacement for the center of the optical trap. Therefore, the spatial distribution of species in the plasma is conditioned by both, the size of the inspected particle and its chemical nature. Higher thermophoretic effects for larger particles as well as for non-metallic samples are relevant for material characterization in techniques involving plasmas as excitation source. The dissemination of emitting atoms can lead to incomplete plasma chemical characterization as these species are

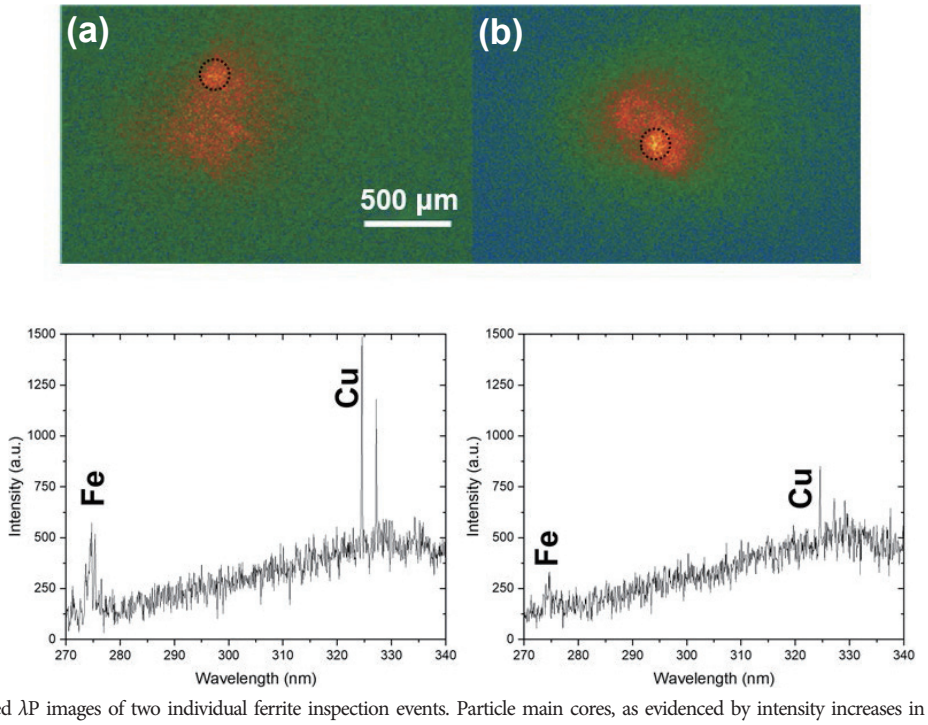

Figure 4 Fully processed λP images of two individual ferrite inspection events. Particle main cores, as evidenced by intensity increases in the particular region of interest, are indicated by the dashed lines. The average length of Cu diffusion clouds was 420 μm, as measured from the center of the core. LIBS spectra associated to each image are provided below. Scale bar is 500 μm.

diluted in ionized air and remain undetected by dispersive spectroscopy. For laser fabrication processes, uneven dissociation may result in larger size distributions linked to the formation of numerous nucleation spots surrounded by different concentrations of the ablated material. In line with these arguments, it is reasonable to hypothesize that different atoms will show particular migration coefficients according to their physical traits such as size, mass, and conductivity. Relocation due to thermophoresis and sequential release of constituent atoms need to be carefully addressed for successfully characterizing the plasma composition as well as to understand possible interactions of the released atoms and the formation of new species within the plasma.

2.3 Detection efficiency and analytical performance of λP-imaging for the chemical characterization of single trapped particles

To rationalize the more tedious process of using of images to yield quantitative information regarding the samples, we compared the detection efficiency of λP-imaging and LIBS. To do so, the emission sensitivity, in photons·g^{-1}, for both detection lines was calculated following the protocol described in Refs. [19, 25]. By calculating the sensitivity of each of the two inspection lines used herein, we were able to evaluate the proficiency of each one for extracting analytical information for the same source, the laser-induced plasma. The employed approach backtracks the photons from the detection system to the laser-induced plasma. For this purpose, the loss of photons along the optical pathway was estimated by considering the transmission and/or reflection of light in each optical component along the full system. In this context, spectrometers are complex devices within which orders of magnitude of photons are lost in order to direct the light into the electronic translator producing the observed signal. The efficiency of the grate separating the convoluted contributions in the plasma is of utmost importance, as is the number of internal mirrors. Moreover, the coupling between the optical fiber and the spectrometer entrance slit hinders photon detection, depending on the aspect ratio between elements, while significant losses may occur.

In our case, with a fixed slit of 100 μm, only 1 out of every 50 photons reach the spectrometer [9]. In the detector, the number of photons to generate a single intensity unit was calculated from $S = \omega d\ (\mathrm{QE}\Psi)^{-1}$. In this expression, S is the detector's sensitivity, ωd is the depth of the pixel well, QE is the detector's quantum efficiency, and Ψ its analog-to-digital (AD) converter (16 bits in our case). This number was then multiplied by the net counts produced by the three samples probed and sequential losses were added to provide the number of photons at the particle spot estimated by each technique. A key point to address was that the full plasma volume was collected in both inspection cases to ensure that measurements were readily comparable. As mentioned above, even in the case of full plasma projection on the tip of the optical fiber used to collect spectroscopic data, the entrance slit of the spectrometer herein used hindered full plasma volume readout. Therefore, this loss must be considered to provide an accurate estimation of LIBS efficiency. Thus, the plasma was considered a point source and the solid angle of the collection bundle was calculated as 0.20 steradian. Then, based on the plasma volume featuring analyte emission, the plasma could be reconstructed as a sphere from the LIBS point of view with photons emitted in every direction being taken into consideration to yield the final calculated efficiency. Lastly, the total photons were normalized to 1 gram of sample for further comparative purposes.

The λP images and the simultaneous LIBS signal were converted into the number of photons reaching the detector, considering the conversion efficiency of both lines at λ = 324.75 nm. As depicted in Fig. 5(a), by accounting for losses along each optical path and the transmittance percentage (%T) for the filters used in each case, the emission sensitivity (or photon budget) was calculated for graphite, Cu NPs, and ferrites. The comparative data for both methodologies are summarized in Table 1. Data featured in Table 1 correspond to the delay time at which the maximum intensity was registered for each detection pathway. As seen in Fig. 4(b), the collection efficiency in the proposed methodology (λP) is three orders of magnitude greater than in dispersive LIBS. This was favored by the circumvention of the optics mentioned above that was high enough to overcome the significant differences found in Ψ for the iCCD camera and the time-integrated spectrometer's CCD, with Ψ_{iCCD} being 0.1 times $\Psi_{\mathrm{spectrometer}}$ at the wavelength range of work (ca. 320–400 nm). Quantum efficiency was, therefore, the main reason limiting the efficiency of λP from being higher, along with increased signal variability due to the size dispersion of the samples. Also, it justified the use of wavelength-specific filters instead of focusing the light directly into the entrance slit for LIBS inspection, a common solution to avoid the restrictions and losses imposed by the use of optical fibers. Another drawback deriving from direct focusing in our particular case would be the loss of NP real-time tracking and reduced spatial resolution and increased operational difficulty for the alignment of the different instrumental lines comprising the whole system, as elaborated in the OC-OT-LIBS setup subsection in Methods. As seen in Fig. 5(a), the number of photons produced by the particle at a given time varied depending on the technique used to calculate it. This was a straightforward consequence of the reduced detection sensitivity of LIBS, which turned the technique blind to the excess of photons being really produced by the samples.

To evaluate the analytical figures of merit tied to λP imaging analysis, LODs for each sample were calculated from the expression $\mathrm{LOD} = 3C\ \mathrm{RSD_B}\ (\mathrm{S/B})^{-1}$ [26, 27], where C is the analyte mass contained within the particle, $\mathrm{RSD_B}$ is the average relative standard deviation for air blanks recorded at d = 800 and 500 ns (for graphite and Cu, respectively), and S/B, the average signal to background ratio. λP experiments lead to LODs of 0.54 fg for graphite and 18 ag for Cu, with these being improvements of three and two times over previously published LIBS LODs, 1.7 fg [19] and 37 ag [9], respectively. Therefore, enhanced sensitivity for λP plasma analysis is demonstrated for the inspection of single nanoparticulate materials.

3 Conclusions

In this work, the authors demonstrate the successful application of time-resolved λP-imaging for the analysis of single trapped nanoparticles in air and atmospheric pressure. λP imaging was performed simultaneously to LIBS. Increases between 4 and 5 orders of magnitude in the number of detected photons, for nano- and microparticles respectively, were calculated when using λP inspection. For the proposed methodology, LODs were calculated to be 0.54 fg for graphite and 18 ag for copper. These results improve upon those previously reported for single nanoparticles using LIBS analysis. Yet, results show that the synergy of λP and LIBS when performed together is not limited to improved chemical characterization of single particles. While LIBS provides enough detection power to identify the main components of the particles and, therefore, select the wavelength regions for λP, the latter allows enhanced detection of the species and the monitoring of processes related to the spatial distribution of the elements. This

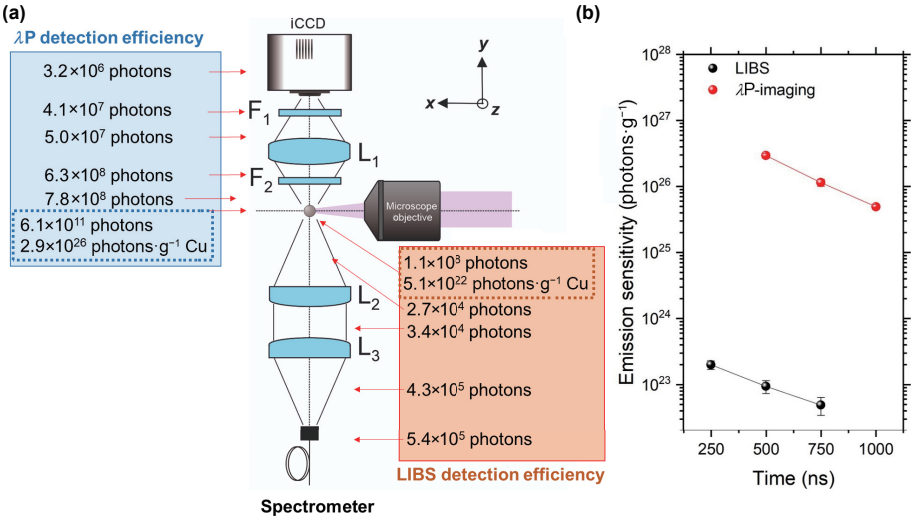

Figure 5 Detection efficiency for single Cu nanoparticles calculated for both characterization lines integrated in the inspection platform. (a) Photon budget calculus scheme for each of the λP-imaging and LIBS lines comparing the number of photons produced by a 90 nm ferrite particle. F_1 corresponds to the SPF in Fig. 1(a) while F_2 is the Cu-LF in the same figure. (b) Evolution of number of photons in time calculated from the Cu signal at each detector for 70 nm Cu NPs. Owing to the higher number of photons collected in the λP line, net Cu emission appeared at a later time due to increased background. Yet, this technique is capable of detecting Cu signal at d = 1000 ns, while emission is considered extinct by LIBS at the same acquisition delay. Points were calculated using the simultaneously acquired data featured in Fig. 3.

Table 1 Calculated number of photons detected by each technique at acquisition time $d = I_{max}$

Species	Photons at the detector (λP)	Photons at the detector (LIBS)
Graphite	$2.98 \times 10^{24} \pm 2.08 \times 10^{23}$	$6.55 \times 10^{19} \pm 3.81 \times 10^{18}$
Cu	$2.93 \times 10^{26} \pm 2.40 \times 10^{25}$	$5.15 \times 10^{22} \pm 7.29 \times 10^{21}$
$CuFe_2O_4$	$4.74 \times 10^{26} \pm 2.03 \times 10^{26}$	$6.82 \times 10^{22} \pm 2.2 \times 10^{22}$

reveals new information inaccessible using only spectroscopic means. Size and chemical bond-dependent biased diffusion within the plasma volume due to heat and momentum transfer to the particles was evidenced by λP imaging. This may be of great interest for researchers in laser activation of nanoprobes or those working in topics related to laser-generation of nanoentities. Understanding the migration of chemical species within the plasma may explain deviations from the target morphology or composition in the materials resulting from laser ablation, especially for multicomponent particles. For example, the several nucleation spots formed during the process may only include neighboring atoms of a given element while neglecting other species or growing in a preferential direction yielding unwanted shapes. By observing the chemical anisotropy in the plasma, corrections may be performed to overcome or exploit the uneven elemental distribution. To the best of our knowledge, this article constitutes the first report on wavelength-resolved direct laser-induced plasma plumes analysis of single trapped nanoparticles with a 100% sampling efficiency. Therefore, we introduce a new tool aimed at extremely precise nanoinspection of a broad variety of nanoparticulate materials.

4 Methods

4.1 OC-OT-λP-LIBS working scheme

The custom-built instrumental used herein allowed working directly with dry powdered samples. Samples were catapulted into aerosol form using a laser-produced shockwave. The employed sampling scheme favored short aerosol relaxation times. Particles flowing within the sample chamber passed through the optical trap eventually becoming isolated. Laser excitation and plasma production were performed only after dual check of the absence of particle collisions via observation with the iCCD camera and an additional CMOS. To align the system, an air plasma was imaged using the iCCD camera to determine the z coordinate at which the trap had to be set to ensure particle–plasma interaction. This point was fixed as the zero spot to which other detection systems were aligned.

4.2 Samples

2 μm graphite (Sigma-Aldrich), 70 and 25 nm Cu, and 90 nm $CuFe_2O_4$ (mkNano) spherical particles were probed by LIBS and λP-imaging analysis. Qualitative sample portions in the microgram range were used for the experiments. Particles were placed on a 200 mm thick cover glass serving as bottom of the sample chamber. Then, a three-dimensional (3D) printed skimmer-like cone was placed upon the particle and fixed on the glass cover using fast-drying glue. As reported in Ref. [10], this scheme leaded to less particle-dense aerosols being catapulted, therefore allowing faster and steadier optical trapping (average time for complete analysis being ca. 3.5 min). Finally, the cone was covered by quartz cuvette also glued into the glass slide to conform the sample chamber. The use of quartz minimized photon absorption by the cuvette's walls as plasma light traversed its way into the detectors. Relevant sample traits are given in Table S1 in the ESM.

4.3 OC-OT-LIBS setup

First, in order to aerosolize the samples via OC, a Nd:YAG ns laser pulse at fundamental wavelength (λ = 1064 nm, τ = 6 ns) was guided by a mirror into the back aperture of a 20× long working distance (WD) microscope objective (MO; 19 mm WD, 0.40 numerical aperture (NA)) placed on a micrometric stage allowing for reposition along the experiment's z-axis. The pulse was focused just below the glass sample platform (described below) to form a laser-induced shockwave that reached the particles and ejected them. The energy of the OC pulses was kept below the MO's damage threshold and the plasma formation threshold for glass, thus ensuring no drilling of the sample chamber. A continuous wave (CW) laser at 532 nm (transverse electromagnetic mode (TEM) 00, 300 mW) was used to setup the optical trap by focusing the light with the same MO employed to guide the OC pulse. Power at the sample plane was P = 180 mW

with a 6.9 μm beam waist at the trap. As the aerosol stream relaxed, single particles entered the trap and OT became stable owing to reduced number of particle collisions. The position of the particles was adjusted by moving the MO along the *z*-axis until placed at the (0, 0, 0) coordinate (referred as zero in Results and discussion section) to which every other component was aligned. This spot corresponded to the superposition in the xy plane of the center of the plasma produced by the inspection laser and the particle and was determined via plasma imaging [19]. Particle excitation was performed using a ns-pulsed laser with λ = 1064 nm (τ = 6 ns, 260 mJ per pulse) focused through a 10× high-power MO (15 mm WD, 0.25 NA) in the *x* axis. The pulse energy used throughout the reported experiments was 260 mJ·pulse^{-1}, leading to an energy density at the (0, 0, 0) spot of 3.3×10^3 J·cm^{-2}. Plasma light for LIBS analysis was collected in the *y* axis by a pair of 2 inches biconvex lenses (FS, 100 mm focal length) focusing the radiation into the tip of a single-channel optical fiber (core diameter 1000 μm) connected to a time-integrated spectrometer (gate width = 1.1 ms). Additionally, a CMOS camera coupled to a 10× MO (17.5 WD, 0.30 NA) in the *x* axis to verify the particle position observed in the iCCD as well as to further confirm no aerosol presence prior to plasma formation. The action of the OC and the LIBS lasers as well as the start of the spectrometer measures were synchronized by a pair of pulse generators. Experiments were always performed in air at atmospheric pressure and room temperature.

4.4 Wavelength-resolved plasma imaging setup

The λP-imaging inspection line located in the *y*-axis is shown in Fig. 1(a). The line consisted of a plano-convex (1 inch in diameter) lens focusing the plasma light into an iCCD camera (Andor iStar DH334T-18U-03). These elements were common for the inspection of both, the micro and the nanoparticles. A filter wheel was placed between both elements containing three different coefficient neutral density (ND) filters, a bandpass filter, a shortpass filter (SPF), and an empty spot allowing for quick exchange of the restriction imposed on the light reaching the detector. ND filters were mainly used for auxiliary plasma imaging diagnostics, i.e., ensuring the system alignment. The bandpass filter centered at λ = 390 nm (FB390-10, Thorlabs) was used for λP-imaging monitoring of the CN emission yielded by graphite particles upon reaction with atmospheric nitrogen. Figure S2(a) in the ESM illustrates the working principle of BP applied to a single-particle LIBS spectrum. In order to inspect single Cu NP plasmas, a combination of two filters was required. First, a line filter, denoted as Cu-LF in Fig. 1, (LL01-325-12.5, Semrock) held by a 360-degree pivoting quick-release mount (Thorlabs) was placed before the focusing lens. By tilting this filter 5°, light at λ = 324.75 nm and photons with λ = 400–900 nm were allowed to pass through it. In order to totally eliminate the contribution of the 400–900 nm wavelength window and obtain clear Cu signal in the recorded plasma images, the shortpass filter (FF01-390/SP-25, Semrock) was used. SPF reflected light outside the ~ 310–380 nm range. Therefore, by applying both filters, only plasma emission at 324.75 nm entered the iCCD detector. Figure S2(b) in the ESM shows the effect of the filter combination on a single Cu nanoparticle LIBS spectrum. Plasma magnification at the camera was 1:1.

4.5 Optical trapping

The setup employed herein allowed for stable trapping in air at atmospheric pressure of up to hours for graphite particles and ca. 10 min for both nanoparticles. Details on particle trapping protocols and quantitative data can be found in previous works by the authors [9, 19, 26]. Briefly, the forces were in the range of few pN·nm^{-1} for the micrometric particles and fN·nm^{-1} for the nanoparticles. Despite these being lower than other quantitative results found in literature for more conventional OT settings [28–33], the forces were enough to allow particle retention for the duration of the experiment as well as manipulation of the particle position until its relocation to zero coordinate for successful inspection. Owing to the steady positioning enabled by OT, the hit ratio for the system, that is, the number of laser shots providing measurable signals for both, λP-imaging and LIBS lines, was of 100%. Therefore, every trapped particle could be successfully analyzed in the instrumental platform.

4.6 LIBS data analysis

To assess whether collected LIBS spectra were ascribed to single particles or to an agglomerate, the sorting method described in Ref. [9] was used. Briefly, owing to the aforementioned proportionality between net LIBS intensity and inspected mass, single particles are expected to yield the smaller signals out of a data series. From spectra of trapped particles, the net values for the CN emission at 388.3 nm and Cu(I) emission at 324.7 nm were calculated. Upon inspection of the data, signal gaps could be observed with value differences ranging from 50% to 100%, outlining that more than one particle were probed. Given the size-dependent seeding effects present in LIBS emission of clustered nanoparticles, cluster events lead to non-linear intensity increases [20, 34]. The combination of seeding effects with not statistically enough cluster events denied the chance of precisely outlining the number of particles comprising the agglomerate, i.e., dimers, trimers or other small clusters. Thus, we divided the intensities in two: a single particle region and an agglomerate region. Weaker net intensities found in the acquired data series were averaged (μ_{events}) to span intensity windows ranging from three times the standard deviation of the background (3s, measured by acquiring LIBS spectra on particle-free sample chambers) up to a maximum value of μ_{events} + 3s. Net intensity values featuring SNR > 3 within the calculated limits were considered to belong to single particles and used for further processing in both LIBS and λP-imaging inspection modes.

For comparison of the detection efficiency, LIBS signal presented corresponded to the integrated area below peak for better comparison to λP-imaging intensity, which resulted from integration of sample-containing pixels. An example of the sorting scheme is shown in Fig. S7 in the ESM.

Furthermore, several graphite-related emissions are included in the λP images to a varying degree owing to the wavelength width of the bandpass filter (Fig. S2 in the ESM), these being the transitions 0-0 (388.3 nm), 1-1 (387.1 nm), and 2-2 (386.19 nm) of the CN (B2Σ-X2Σ) system, and net LIBS intensity data for graphite microparticles shown in Fig. 2 and discussed in Results and discussion section were calculated as Net I_{CN} = ΣNet $I_{0\text{-}0,1\text{-}1,2\text{-}2}$. To obtain Net I_{CN}, background intensity was acquired for at each delay value in the signal-less region between 370 and 375 nm (Fig. S2(a) in the ESM), which featured identical detector efficiency as the 380–395 nm window used for particle monitoring (Fig. S4 in the ESM).

4.7 Image data analysis

Once raw plasma images were acquired, processing and treatment of the λP-imaging data were performed using the Fiji/ImageJ open-source software. In a first step, the contribution from the concomitant air plasma was subtracted. For this purpose, empty sampling chambers were used for recording analyte-free air plasmas serving as blanks. Once the background had been corrected, a Gaussian smoothing and red/green/blue (RGB) color palette was applied to produce the final λP images, thus yielding

the complete contribution of the inspected particles within the plasma.

An image processing algorithm was also implemented in Fiji/ImageJ [35, 36] software for quantitative data. The algorithm allowed establishing the maximum and minimum intensity values in the histogram of the plasma images, adjusting the thresholds values in a later stage, and selecting the area of interest over which the quantification script was to be run. Prior to the extraction of numeric data from the images, intensity values below 0 were forced to equal 0 (if $I < 0$, $I = 0$) to avoid signal loss and increased uncertainty owing to isolated pixels encircled within the particle-related image area. The algorithm provided the integrated area, i.e., the net analyte signal used for discussion, the average intensity, and the standard deviation from the area of interest, which was averaged for multiple images in order to calculate the reported limits of detection.

Acknowledgements

Research is funded by the Spanish Ministerio de Economia y Competitividad (Nos. CTQ2017-82137P and CTQ2014-56058P). P. P. is grateful to the European Union's NextGenerationEU plan and the Spanish Ministerio de Universidades for his Margarita Salas fellowship under the program "Ayudas para la recualificación del Sistema Universitario español". Authors are grateful to the Universidad de Málaga/CBUA for fundings for open access charges.

Funding note: Open Access funding provided thanks to the CRUE-CSIC agreement with Springer Nature.

Electronic Supplementary Material: Supplementary material (containing expanded description on the experimental setup used, LIBS spectra, and full temporal evolution of wavelength resolved imaging series) is available in the online version of this article at https://doi.org/10.1007/s12274-022-5355-3.

References

[1] Jørgensen, J. T.; Norregaard, K.; Tian, P. F.; Bendix, P. M.; Kjaer, A.; Oddershede, L. B. Single particle and PET-based platform for identifying optimal plasmonic nano-heaters for photothermal cancer therapy. *Sci. Rep.* **2016**, *6*, 30076.

[2] Jauffred, L.; Samadi, A.; Klingberg, H.; Bendix, P. M.; Oddershede, L. B. Plasmonic heating of nanostructures. *Chem. Rev.* **2019**, *119*, 8087–8130.

[3] Liu, Q.; Zhang, Y. X.; Peng, C. S.; Yang, T. S.; Joubert, L. M.; Chu, S. Single upconversion nanoparticle imaging at sub-10 W cm^{-2} irradiance. *Nat. Photonics* **2018**, *12*, 548–553.

[4] Prigozhin, M. B.; Maurer, P. C.; Courtis, A. M.; Liu, N.; Wisser, M. D.; Siefe, C.; Tian, B.; Chan, E.; Song, G. S.; Fischer, S. et al. Bright sub-20-nm cathodoluminescent nanoprobes for electron microscopy. *Nat. Nanotechnol.* **2019**, *14*, 420–425.

[5] Kohli, R. K.; Davies, J. F. Measuring the chemical evolution of levitated particles: A study on the evaporation of multicomponent organic aerosol. *Anal. Chem.* **2021**, *93*, 12472–12479.

[6] Wang, X. D.; Zhang, X. R.; Huang, D. X.; Zhao, T. Y.; Zhao, L. L.; Fang, X. K.; Yang, C. H.; Chen, G. Y. High-sensitivity sensing of divalent copper ions at the single upconversion nanoparticle level. *Anal. Chem.* **2021**, *93*, 11686–11691.

[7] Liu, C.; Zheng, X. C.; Dai, T. T.; Wang, H. L.; Chen, X.; Chen, B.; Sun, T. Y.; Wang, F.; Chu, S.; Rao, J. H. Reversibly photoswitching upconversion nanoparticles for super-sensitive photoacoustic molecular imaging. *Angew. Chem., Int. Ed.* **2022**, *61*, e202116802.

[8] Swearer, D. F.; Fischer, S.; Angell, D. K.; Siefe, C.; Alivisatos, A. P.; Chu, S.; Dionne, J. A. Single particle cathodoluminescence spectroscopy with sub-20 nm, electron-stable phosphors. *ACS Photonics* **2021**, *8*, 1539–1547.

[9] Purohit, P.; Fortes, F. J.; Laserna, J. J. Spectral identification in the attogram regime through laser-induced emission of single optically trapped nanoparticles in air. *Angew. Chem., Int. Ed.* **2017**, *56*, 14178–14182.

[10] Purohit, P.; Fortes, F. J.; Laserna, J. J. Subfemtogram simultaneous elemental detection in multicomponent nanomatrices using laser-induced plasma emission spectroscopy within atmospheric pressure optical traps. *Anal. Chem.* **2019**, *91*, 7444–7449.

[11] Purohit, P.; Fortes, F. J.; Laserna, J. J. Optical trapping as a morphologically selective tool for *in situ* LIBS elemental characterization of single nanoparticles generated by laser ablation of bulk targets in air. *Anal. Chem.* **2021**, *93*, 2635–2643.

[12] Jolivet, L.; Catita, L.; Delpoux, O.; Lienemann, C. P.; Sorbier, L.; Motto-Ros, V. Direct multi-elemental imaging of freshly impregnated catalyst by laser-induced breakdown spectroscopy. *J. Catal.* **2021**, *401*, 183–187.

[13] Kunjachan, S.; Detappe, A.; Kumar, R.; Ireland, T.; Cameron, L.; Biancur, D. E.; Motto-Ros, V.; Sancey, L.; Sridhar, S.; Makrigiorgos, G. M. et al. Nanoparticle mediated tumor vascular disruption: A novel strategy in radiation therapy. *Nano Lett.* **2015**, *15*, 7488–7496.

[14] Sancey, L.; Kotb, S.; Truillet, C.; Appaix, F.; Marais, A.; Thomas, E.; van der Sanden, B.; Klein, J. P.; Laurent, B.; Cottier, M. et al. Long-term *in vivo* clearance of gadolinium-based AGuIX nanoparticles and their biocompatibility after systemic injection. *ACS Nano* **2015**, *9*, 2477–2488.

[15] Nardecchia, A.; de Juan, A.; Motto-Ros, V.; Gaft, M.; Duponchel, L. Data fusion of LIBS and PIL hyperspectral imaging: Understanding the luminescence phenomenon of a complex mineral sample. *Anal. Chim. Acta* **2022**, *1192*, 339368.

[16] Negre, E.; Motto-Ros, V.; Pelascini, F.; Yu, J. Classification of plastic materials by imaging laser-induced ablation plumes. *Spectrochim. Acta Part B At. Spectrosc.* **2016**, *122*, 132–141.

[17] Vogt, D. S.; Schröder, S.; Frohmann, S.; Hansen, P. B.; Seel, F.; Gensch, M.; Hübers, H. W. Spatiotemporal characterization of the laser-induced plasma plume in simulated Martian conditions. *Spectrochim. Acta Part B At. Spectrosc.* **2022**, *187*, 106326.

[18] Hohreiter, V.; Hahn, D. W. Plasma–particle interactions in a laser-induced plasma: Implications for laser-induced breakdown spectroscopy. *Anal. Chem.* **2006**, *78*, 1509–1514.

[19] Purohit, P.; Fortes, F. J.; Laserna, J. J. Atomization efficiency and photon yield in laser-induced breakdown spectroscopy analysis of single nanoparticles in an optical trap. *Spectrochim. Acta Part B At. Spectrosc.* **2017**, *130*, 75–81.

[20] Fortes, F. J.; Purohit, P.; Laserna, J. J. Energy transfer mechanisms in laser-induced plasmas: Variation of physical traits mediated by the presence of single optically-trapped nanoparticulate material. *Spectrochim. Acta Part B At. Spectrosc.* **2021**, *180*, 106193.

[21] Harilal, S. S.; Issac, R. C.; Bindhu, C. V.; Gopinath, P.; Nampoori, V. P. N.; Vallabhan, C. P. G. Time resolved study of CN band emission from plasma generated by laser irradiation of graphite. *Spectrochim. Acta Part A Mol. Biomol. Spectrosc.* **1997**, *53*, 1527–1536.

[22] Harilal, S. S.; Bindhu, C. V.; Nampoori, V. P. N.; Vallabhan, C. P. G. Influence of ambient gas on the temperature and density of laser produced carbon plasma. *Appl. Phys. Lett.* **1998**, *72*, 167–169.
[23] Schoolcraft, T. A.; Constable, G. S.; Zhigilei, L. V.; Garrison, B. J. Molecular dynamics simulation of the laser disintegration of aerosol particles. *Anal. Chem.* **2000**, *72*, 5143–5150.
[24] Zhigilei, L. V.; Garrison, B. J. Computer simulation study of damage and ablation of submicron particles from short-pulse laser irradiation. *Appl. Surf. Sci.* **1998**, *127–129*, 142–150.
[25] Fortes, F. J.; Fernández-Bravo, A.; Laserna, J. J. Chemical characterization of single micro- and nano-particles by optical catapulting-optical trapping-laser-induced breakdown spectroscopy. *Spectrochim. Acta Part B At. Spectrosc.* **2014**, *100*, 78–85.
[26] Hahn, D. W.; Omenetto, N. Laser-induced breakdown spectroscopy (LIBS), Part I: Review of basic diagnostics and plasma-particle interactions: Still-challenging issues within the analytical plasma community. *Appl. Spectrosc.* **2010**, *64*, 335A–336A.
[27] Hahn, D. W.; Omenetto, N. Laser-induced breakdown spectroscopy (LIBS), Part II: Review of instrumental and methodological approaches to material analysis and applications to different fields. *Appl. Spectros.* **2012**, *66*, 347–419.
[28] Purohit, P.; Samadi, A.; Bendix, P. M.; Laserna, J. J.; Oddershede, L. B. Optical trapping reveals differences in dielectric and optical properties of copper nanoparticles compared to their oxides and ferrites. *Sci. Rep.* **2020**, *10*, 1198.
[29] Samadi, A.; Klingberg, H.; Jauffred, L.; Kjær, A.; Bendix, P. M.; Oddershede, L. B. Platinum nanoparticles: A non-toxic, effective and thermally stable alternative plasmonic material for cancer therapy and bioengineering. *Nanoscale* **2018**, *10*, 9097–9107.
[30] Samadi, A.; Bendix, P. M.; Oddershede, L. B. Optical manipulation of individual strongly absorbing platinum nanoparticles. *Nanoscale* **2017**, *9*, 18449–18455.
[31] Hansen, P. M.; Bhatia, V. K.; Harrit, N.; Oddershede, L. Expanding the optical trapping range of gold nanoparticles. *Nano Lett.* **2005**, *5*, 1937–1942.
[32] Righini, M.; Volpe, G.; Girard, C.; Petrov, D.; Quidant, R. Surface Plasmon optical tweezers: Tunable optical manipulation in the femtonewton range. *Phys. Rev. Lett.* **2008**, *100*, 186804.
[33] Juan, M. L.; Righini, M.; Quidant, R. Plasmon nano-optical tweezers. *Nat. Photonics* **2011**, *5*, 349–356.
[34] Dell'Aglio, M.; Alrifai, R.; De Giacomo, A. Nanoparticle enhanced laser induced breakdown spectroscopy (NELIBS), a first review. *Spectrochim. Acta Part B At. Spectrosc.* **2018**, *148*, 105–112.
[35] Abràmoff, M. D.; Magalhães, P. J.; Ram, S. J. Image processing with ImageJ. *Biophotonics Int.* **2007**, *11*, 36–42.
[36] Schneider, C. A.; Rasband, W. S.; Eliceiri, K. W. NIH image to ImageJ: 25 years of image analysis. *Nat. Methods* **2012**, *9*, 671–675.